Article

Discovery Medicine 2026; 38(208): 1403–1416
https://doi.org/10.24976/Discov.Med.202638208.110

The Immunosuppressive Checkpoint B7-H3 (CD276) Promotes Ferroptosis Resistance via AKT–SREBP2–Driven Cholesterol Metabolism in Colorectal Cancer

Cuiping Li[1,2], Qin Jin[1], Yuying Sun[1,3], Qing Zhang[1,*]

[1]Department of Pathology, Affiliated Hospital of Nantong University, 226001 Nantong, Jiangsu, China
[2]Department of Pathology, Qingxian People's Hospital, 062650 Qingxian, Hebei, China
[3]Medical School, Nantong University, 226001 Nantong, Jiangsu, China
*Correspondence: tdfyzhangqing@sina.com (Qing Zhang)
Submitted: 5 March 2026 Revised: 3 April 2026 Accepted: 9 April 2026 Published: 20 May 2026

Background: Colorectal cancer (CRC) remains one of the most prevalent malignancies worldwide. Ferroptosis, a form of regulated cell death driven by lipid peroxidation, has emerged as a critical determinant of tumor progression, particularly through its interplay with dysregulated cholesterol metabolism. However, the role of the immune checkpoint molecule B7-H3 (CD276) in regulating ferroptosis in CRC remains poorly defined. This study aimed to characterize the expression profile of B7-H3 in CRC and elucidate its role and underlying mechanisms in ferroptosis regulation, with a focus on cholesterol metabolic signaling.

Methods: B7-H3 expression was assessed in normal colonic epithelial cells and CRC cell lines by Western blotting. Stable CD276 knockdown and overexpression models were established using lentiviral transduction. Ferroptosis sensitivity was evaluated using Cell Counting Kit-8 (CCK-8) assays following RSL3 treatment, along with measurements of malondialdehyde (MDA), intracellular Fe^{2+} levels, and ferroptosis-related gene expression. Cholesterol metabolism was assessed by quantifying total cholesterol (TC) and low-density lipoprotein cholesterol (LDL-C) levels. Activation of the AKT–SREBP2 signaling axis was examined using Western blotting. Mechanistic validation was performed using the SREBP2 inhibitor betulin and the AKT inhibitor perifosine. An *in vivo* xenograft model under a high-cholesterol diet was further employed to evaluate the role of B7-H3 in tumor growth and regulation of ferroptosis.

Results: B7-H3 expression was significantly elevated in CRC cell lines (RKO, HCT116, SW480) compared with normal NCM460 cells ($p < 0.001$), with the highest expression observed in HCT116 cells. Stable CD276 knockdown and overexpression models were successfully established ($p < 0.001$). CD276 silencing markedly reduced cell viability, enhanced ferroptosis sensitivity, and increased levels of MDA, Fe^{2+}, TC, and LDL-C ($p < 0.05$), accompanied by upregulation of PTGS2, FTL, and FTH mRNA ($p < 0.001$) and downregulation of glutathione peroxidase 4 (GPX4) ($p < 0.05$). In contrast, CD276 overexpression produced the opposite phenotype and significantly protected cells from RSL3-induced viability loss ($p < 0.001$). Mechanistically, CD276 knockdown increased nuclear SREBP2 (n-SREBP2) levels while reducing the p-AKT/AKT ratio ($p < 0.001$), whereas CD276 overexpression showed the opposite effect ($p < 0.01$). Betulin significantly reversed the elevation in TC, LDL-C, MDA, and Fe^{2+} induced by CD276 knockdown ($p < 0.001$), while perifosine restored n-SREBP2 expression that had been suppressed by CD276 overexpression ($p < 0.01$). *In vivo*, under a high-cholesterol diet, CD276 knockdown significantly reduced tumor volume and weight ($p < 0.01$), while increasing SREBP2 and COX-2 staining intensity, as well as MDA and Fe^{2+} levels in tumor tissues ($p < 0.001$).

Conclusions: B7-H3 is upregulated in CRC and promotes tumor progression by suppressing ferroptosis through modulation of the AKT–SREBP2 axis and cholesterol metabolism. Targeting B7-H3 may represent a promising therapeutic strategy to induce SREBP2-dependent ferroptosis in colorectal cancer.

Keywords: colorectal cancer; CD276; ferroptosis; cholesterol metabolism; AKT–SREBP2 axis

Introduction

Colorectal cancer (CRC) is a highly prevalent malignant tumor with substantial mortality worldwide, accounting for approximately 1.9 million new cases and 935,000 deaths globally in 2020 [1]. In China, there were an estimated 517,000 new cases of CRC and 240,000 related deaths in 2022 [2], with incidence rising annually, driven by the adoption of westernized lifestyles and population aging. While multimodal management strategies, including endoscopic screening, surgical resection, chemoradiotherapy, and targeted therapy, are widely implemented in clinical practice, the prognosis of patients with advanced CRC remains dismal, with a 5-year overall survival rate of only ~13% among those with distant metastasis [3]. Conventional chemotherapy is hampered by high systemic toxicity, limited efficacy, and frequent acquisition of drug resistance [3,4]. Targeted agents, such as anti-EGFR and anti-VEGF therapies, also face persistent challenges of acquired resistance and disease recurrence, highlighting an urgent need to identify novel therapeutic targets and cell death mechanisms to overcome current therapeutic bottlenecks in CRC.

Ferroptosis is a form of regulated cell death driven by iron-dependent peroxidation of polyunsaturated fatty acids in cellular membranes [5,6]. Induction of ferroptosis in tumor cells has emerged as a promising strategy to effectively suppress tumor growth and overcome resistance to chemotherapy and targeted therapies [7]. While lipid peroxidation and iron metabolism constitute the core regulatory axes of ferroptosis [5], emerging evidence has revealed that cholesterol metabolism can modulate ferroptosis susceptibility by tuning the abundance of endogenous antioxidant molecules, including coenzyme Q10 (CoQ10) and squalene [8]. However, the upstream regulatory molecules and mechanistic networks governing ferroptosis in CRC remain incompletely characterized, and targeting ferroptosis represents an emerging, high-potential direction for CRC treatment.

B7-H3 (also designated *CD276*) is a type I transmembrane immunoregulatory protein of the B7 family, which is frequently overexpressed in a broad spectrum of human malignancies but exhibits restricted, low-level expression in normal tissues [9]. Its aberrant upregulation is tightly associated with malignant progression, enhanced tumor cell proliferation and invasive capacity, and inferior clinical outcomes across multiple cancer types [10]. In CRC, specifically, high B7-H3 expression is similarly correlated with augmented proliferative and invasive phenotypes of tumor cells, as well as significantly reduced patient survival [11]. However, existing studies on B7-H3 in CRC have predominantly focused on its immunoregulatory and pro-proliferative functions. Whether B7-H3 participates in ferroptosis regulation and whether it engages in crosstalk with cholesterol metabolism to modulate ferroptosis susceptibility has not been reported to date.

The AKT signaling cascade is a canonical pro-oncogenic axis that transduces extracellular stimuli to promote tumor cell proliferation, migration, and apoptosis resistance, as well as to orchestrate cellular energy metabolism [12]. Its downstream transcription factor, sterol regulatory element-binding protein 2 (SREBP2), is the master regulator of cholesterol biosynthesis, driving cholesterol synthesis and uptake via transcriptional upregulation of key effectors, including 3-hydroxy-3-methylglutaryl-coenzyme A (HMG-CoA) reductase and low-density lipoprotein (LDL) receptor [13]. Dysregulated cholesterol metabolism is not only causally implicated in tumor initiation and progression, but also directly modulates cellular susceptibility to ferroptosis: reduced cholesterol levels alter the intracellular accumulation of antioxidant species, such as CoQ10 and squalene, thereby increasing cellular vulnerability to ferroptosis [8]. However, whether B7-H3 modulates cholesterol metabolism through the AKT/SREBP2 axis, and thereby shapes ferroptosis tolerance in CRC cells, remains a critical unresolved scientific question.

Here, we aimed to delineate the functional role and underlying mechanistic basis of B7-H3 (*CD276*) in regulating ferroptosis in CRC cells. *In vitro*, we employed RNA interference-mediated knockdown or enforced overexpression of *CD276* to examine its effects on ferroptosis markers, cholesterol metabolism profiles, and AKT/SREBP2 signaling axis activity. Mechanistically, we validated whether B7-H3 (*CD276*) governs cholesterol metabolism via AKT activation-mediated suppression of SREBP2 activity. *In vivo*, we used a high-cholesterol diet-fed nude mouse xenograft model to verify the impact of *CD276* targeting on CRC tumor growth and ferroptosis susceptibility. Collectively, our study fills a critical gap in understanding the functional link between B7-H3 (*CD276*), ferroptosis, and cholesterol metabolism, and identifies a novel molecular target and potential therapeutic strategy for CRC.

Materials and Methods

Cell Lines and Culture Conditions

The human normal colonic epithelial cell line NCM460 (INCELL, San Antonio, TX, USA; Cat. No. NCM460D), colorectal cancer cell lines RKO (TCHu116), HCT116 (TCHu99), and SW480 (TCHu172) were obtained from the Cell Bank of the Chinese Academy of Sciences (Shanghai, China). All cell lines were authenticated by short tandem repeat (STR) profiling ($\geq$98% match) and tested negative for mycoplasma contamination by PCR (detection limit $<10^2$ CFU/mL). NCM460 cells were cultured in DMEM/F12 medium (Gibco, 11330-032) supplemented with 10% fetal bovine serum (FBS; Gibco, 10099-141) and penicillin–streptomycin (Gibco, 15140-122). RKO, HCT116, and SW480 cells were maintained in RPMI 1640 medium (Gibco, 11875-093) with the same supplements as described above. All cells were incubated at 37 °C in a

humidified atmosphere containing 5% CO_2 and passaged every 2–3 days using 0.25% trypsin–EDTA (Gibco, 25200-056). Cells in the logarithmic growth phase were used for all experiments.

Generation of Stable Cell Lines

Short hairpin RNA (shRNA) targeting *CD276* (5′-GTGCTGGAGAAAGATCAAA-3′) and a non-targeting control (5′-GTTCTCCGAACGTGTCACGT-3′) were synthesized by GenePharma (Suzhou, China) and cloned into the pLKO.1-puro vector (Addgene #8453; AgeI/EcoRI sites). The coding sequence (CDS) of human *CD276* (NM_001024735.3) was amplified by PCR and inserted into the pCDH-CMV-MCS-EF1-copGFP vector (System Biosciences, CD511B-1; XbaI/BamHI sites) to generate the overexpression construct (OE-*CD276*), with the empty vector serving as a control (OE-NC). All constructs were verified by Sanger sequencing. For lentivirus production, recombinant plasmids were co-transfected with psPAX2 (Addgene #12260) and pMD2.G (Addgene #12259) into HEK293T cells (ATCC, CRL-3216) at a ratio of 4:3:2 using Lipofectamine 3000 (Thermo Fisher Scientific, L3000015). Viral supernatants were collected 48 h post-transfection, filtered through a 0.45 µm membrane (Millipore, SLGP033RB), and used to infect HCT116 and RKO cells. Stable cell lines were selected with puromycin (2 µg/mL; Sigma-Aldrich, P8833) for 7 days. Knockdown and overexpression efficiencies were validated by Western blotting and qPCR.

HEK293T cells are SV40 large T antigen–transformed human embryonic kidney cells. STR profiling showed a 99.5% match, and mycoplasma contamination was excluded by qPCR within one week prior to experimentation (detection limit $<10^2$ CFU/mL).

Western Blot Analysis

Cells or tissues were lysed on ice for 30 min in RIPA buffer (Beyotime, P0013B) supplemented with protease and phosphatase inhibitors (Roche, 04693159001 and 04906837001), followed by centrifugation at 12,000 ×g for 15 min at 4 °C. For nuclear protein extraction, cells were harvested and resuspended in hypotonic buffer (Beyotime, P0027), incubated on ice for 15 min, and lysed by adding detergent solution with vigorous vortexing for 10 s. The lysates were centrifuged at 12,000 ×g for 10 s at 4 °C to pellet nuclei. The nuclear pellet was then resuspended in nuclear extraction buffer (Beyotime, P0027), incubated on ice for 30 min with occasional vortexing, and centrifuged at 12,000 ×g for 10 min at 4 °C to obtain the supernatant containing nuclear proteins. Protein concentrations were determined using a BCA assay kit (Thermo Fisher Scientific, 23227). Equal amounts of protein (30–50 µg) were separated by 10% SDS-PAGE and transferred onto PVDF membranes (Millipore, IPVH00010). Membranes were blocked with 5% non-fat milk for 1 h at room temperature and incubated overnight at 4 °C with primary antibodies against B7-H3 (Abcam, ab134161, 1:1000), SREBP2 (Abcam, ab30682, 1:1000), phospho-AKT (Cell Signaling Technology, 4060, 1:1000), AKT (Cell Signaling Technology, 4691, 1:1000), and GAPDH (Cell Signaling Technology, 5174, 1:1000). After washing, membranes were incubated with HRP-conjugated secondary antibody (Cell Signaling Technology, 7074, 1:5000) for 1 h at room temperature. Protein bands were visualized using an ECL detection kit (Thermo Fisher Scientific, 32106) and imaged with a ChemiDoc XRS+ system (Bio-Rad). Band intensities were quantified using ImageJ software (version 1.53c; National Institutes of Health, Bethesda, MD, USA) and normalized to GAPDH.

Quantitative Real-Time PCR (qPCR)

Total RNA was extracted using TRIzol reagent (Invitrogen, 15596026), and RNA concentration and purity were assessed using a NanoDrop 2000 spectrophotometer. Complementary DNA (cDNA) was synthesized from 1 µg RNA using the PrimeScript RT reagent kit (Takara, RR037A). Quantitative PCR was performed using TB Green Premix Ex Taq II (Takara, RR820A) on an ABI 7500 Real-Time PCR System. Each 20 µL reaction contained 10 µL 2× SYBR Green Master Mix, 0.4 µL of forward and reverse primers, 2 µL cDNA, and nuclease-free water. The amplification conditions were as follows: initial denaturation at 95 °C for 30 s, followed by 40 cycles of 95 °C for 5 s and 60 °C for 34 s. Relative mRNA expression levels of *CD276*, *PTGS2*, *FTL*, *FTH*, and *GPX4* were calculated using the $2^{-\Delta\Delta Ct}$ method, with GAPDH as the internal control.

Primer sequences (5′→ 3′):

CD276-F: AGCTGTGAGGAGGAGAATGC
CD276-R: TGCTGTCAGAGTGTTTCAGAGG
PTGS2-F: CGGTGAAACTCTGGCTAGACAG
PTGS2-R: GCAAACCGTAGATGCTCAGGGA
FTL-F: CAGCCTGGTCAATTTGTACCT
FTL-R: GCCAATTCGCGGAAGAAGTG
FTH-F: AGTCGTCGGGGTTTCCT
FTH-R: GAGGGTGCGGTGAAGAG
GPX4-F: CAGTTCGGGAAGCAGGAG
GPX4-R: GCCCTTGGGTTGGATCTT

Observation of Mitochondrial Ultrastructure by Transmission Electron Microscopy (TEM)

Cells from each group were harvested, digested with trypsin, and centrifuged to collect cell pellets. Samples were pre-fixed with 3% glutaraldehyde at 4 °C, followed by post-fixation with 1% osmium tetroxide (Cat. No. GP18456, Leica, Germany). After gradient dehydration with acetone, the samples were infiltrated, embedded and polymerized using an Epon 812 epoxy resin embedding kit (Cat. No. GP18010, Beijing Zhongjingkeyi Technology Co., Ltd., China). Ultrathin sections (50 nm thick) were prepared with an EM UC7 ultramicrotome (Leica,

Germany), then underwent double staining with uranyl acetate (Cat. No. GS02624, Beijing Zhongjingkeyi Technology Co., Ltd., China) and lead citrate staining solution (Cat. No. GZ02616, Beijing Zhongjingkeyi Technology Co., Ltd., China). The mitochondrial ultrastructure was observed and images were acquired using a JEM-1400PLUS transmission electron microscope (JEOL Ltd., Japan).

Cell Viability Assay (CCK-8)

Cells were seeded into 96-well plates (Corning) at a density of 5×10^3 cells per well and cultured for 24 h prior to treatment. Subsequently, 10 µL of CCK-8 reagent (Dojindo, CK04) was added to each well and incubated at 37 °C for 1–2 h. Absorbance was measured at 450 nm using a BioTek Synergy H1 microplate reader. Cell viability was calculated as:

$$\text{viability (\%)} = \text{(OD treated / OD control)} \times 100\%.$$

Assessment of Ferroptosis-Related Indicators

Lipid peroxidation was quantified by measuring malondialdehyde (MDA) using a lipid peroxidation assay kit (Beyotime, S0131S). Intracellular Fe^{2+} levels were determined using an iron assay kit (Abcam, ab83366), following the manufacturer's instructions. Absorbance was measured at 532 nm (MDA) and 562 nm (Fe^{2+}). MDA levels were normalized to total protein content, and Fe^{2+} concentrations were calculated based on standard curves. Results are expressed as µmol per mg protein.

Measurement of Cholesterol Metabolism

Total cholesterol (TC; Applygen, E1015) and low-density lipoprotein cholesterol (LDL-C; Applygen, E1018) were quantified using colorimetric assay kits. Cell lysates were centrifuged, and the supernatants were incubated with the working reagents at 37 °C. Absorbance was measured at 500 nm (TC) and 546 nm (LDL-C). Concentrations were calculated from standard curves. Serum samples were expressed as mmol/L, whereas cellular or tissue samples were normalized to protein content (mmol/mg protein).

Inhibitor Treatment Assays

Stable cell lines were seeded into 6-well plates (Corning) and treated at 60–70% confluence. sh*CD276* cells were treated with the SREBP2 inhibitor betulin (MedChemExpress, HY-N0083) at 10–20 µM for 24–48 h. OE-*CD276* cells were treated with the AKT inhibitor perifosine (MedChemExpress, HY-50909) at 5–10 µM for 24–48 h.

For ferroptosis rescue experiments, cells were pretreated with the ferroptosis inhibitor Ferrostatin-1 (Fer-1; MedChemExpress, HY-100579) at 5 µM for 2 h, followed by stimulation with the ferroptosis inducer RSL3 (MedChemExpress, HY-100218A) at 2.5 µM for 24 h. Control cells received an equal volume of DMSO (Sigma-Aldrich, D2650). Cells were harvested for subsequent analyses.

Measurement of PI3K p85α Levels

PI3K p85α levels were determined using a Human PI 3 Kinase p85 alpha ELISA kit (Abcam, ab318932) according to the manufacturer's protocol. Cell lysates were added to microplate wells and incubated at 37 °C, followed by sequential addition of detection antibodies and HRP conjugates. Absorbance was measured at 450 nm, and relative protein levels were calculated based on standard curves.

Co-Immunoprecipitation (Co-IP)

Cells were lysed in IP lysis buffer (Pierce, Cat. No. 87787) supplemented with protease and phosphatase inhibitor cocktails. For immunoprecipitation, 1 mg of precleared cell lysate was incubated overnight at 4 °C with gentle rotation with anti-Flag M2 antibody (Sigma-Aldrich, Cat. No. F1804, 2–4 µg per sample) or anti-PI3K p85 antibody (Cell Signaling Technology, Cat. No. 4292, 2–4 µg per sample). Normal mouse IgG (Santa Cruz Biotechnology, Cat. No. sc-2025) or normal rabbit IgG (Santa Cruz Biotechnology, Cat. No. sc-2027) at the same concentration served as negative controls. Subsequently, Protein A/G magnetic beads (Thermo Fisher Scientific, Cat. No. 88803) were added and incubated for 2 h at 4 °C. The beads were washed four times with IP lysis buffer, and bound proteins were eluted with 2× Laemmli sample buffer for Western blot analysis of B7-H3 (*CD276*) (1:1000), PI3K p85 (1:1000) and Flag tag (1:5000).

Xenograft Tumor Model

All animal experiments were conducted in accordance with institutional guidelines and approved by the Institutional Animal Care and Use Committee of the Affiliated Hospital of Nantong University (Approval No. 2025-L139). Male BALB/c nude mice (4–6 weeks old; Vital River, Beijing, China) were housed under specific pathogen-free conditions and acclimated for 3 days.

To establish a high-cholesterol model, 12 mice were randomly divided into two groups (n = 6 per group) and fed either a standard diet or a high-cholesterol diet (1.25%; Research Diets, D12108C) for 27 days. Serum and hepatic TC levels, as well as serum LDL-C, were measured to confirm model establishment.

For tumor xenografts, HCT116 cells stably expressing shNC or sh*CD276* (5×10^6 cells per mouse, n = 6) were resuspended in pre-chilled serum-free PBS (Gibco, 10010023) and subcutaneously injected into the dorsal flank. Mice were switched to a high-cholesterol diet 3 days post-inoculation. Tumor volumes were measured every 3 days starting from day 7 using the formula:

$$V = 0.5 \times L \times W^2.$$

Mice were euthanized on day 27 by intraperitoneal injection of 0.3% pentobarbital sodium (BSZH Scientific

Inc., P3761) at a dose of 100 mg/kg, and tumors were excised, weighed, and photographed. Portions of tumor tissues were fixed in 4% paraformaldehyde (Servicebio, G1101) for immunohistochemistry, while the remaining tissues were snap-frozen in liquid nitrogen and stored at –80 °C.

Immunohistochemistry (IHC)

Tumor tissues were fixed in 4% paraformaldehyde (Servicebio, G1101) for 24 h, embedded in paraffin, and sectioned at 4 µm thickness. After deparaffinization and rehydration, endogenous peroxidase activity was blocked with 3% hydrogen peroxide (Servicebio, G0114) for 10 min at room temperature. Antigen retrieval was performed using citrate buffer (pH 6.0; Servicebio, G1202).

Sections were blocked with 5% bovine serum albumin (BSA; Servicebio, G5001) for 30 min and incubated overnight at 4 °C with primary antibodies against SREBP2 (Proteintech, 14508-1-AP, 1:200) and COX-2 (Cell Signaling Technology, 12282, 1:200). After washing, sections were incubated with HRP-conjugated secondary antibody (Servicebio, GB23303) for 30 min at room temperature. Staining was visualized using a DAB kit (Servicebio, G1212), followed by hematoxylin counterstaining (Servicebio, G1004). Slides were dehydrated, cleared, and mounted with neutral resin (Solarbio, G8590), and images were captured using an Olympus BX53 microscope.

The protein expression was semi-quantified by Immunoreactive Score (IRS). Two blinded pathologists independently scored 5 random 400× high-power fields per section. IRS was calculated as staining intensity (0–3: negative, weak, moderate, strong) multiplied by positive cell percentage (0–4: <5%, 5%–25%, 26%–50%, 51%–75%, >75%), with a total score of 0–12. The mean IRS per section was used for statistical comparison between the shNC and sh*CD276* groups.

Statistical Analysis

All *in vitro* experiments were independently repeated at least three times. Data are presented as mean ± standard error of the mean (SEM). Statistical analyses were performed using GraphPad Prism 9.0 (GraphPad Software, San Diego, CA, USA). Comparisons between two groups were conducted using unpaired Student's *t*-tests, while multiple-group comparisons were performed using one-way ANOVA followed by Tukey's post hoc test. Tumor growth curves were analyzed using two-way ANOVA to assess time effects, group effects, and their interaction. A two-sided $p < 0.05$ was considered statistically significant.

Results

B7-H3 Is Highly Expressed in CRC Cell Lines, and Stable Knockdown Is Efficient

To investigate the role of B7-H3 in colorectal cancer (CRC), we first examined its expression in normal colonic epithelial cells and CRC cell lines. Western blot analysis revealed that B7-H3 protein levels were markedly elevated in RKO, HCT116, and SW480 cells compared with NCM460 cells ($p < 0.001$; Fig. 1A). Among these, HCT116 exhibited the highest expression, followed by RKO and SW480 (RKO vs HCT116, $p < 0.05$; RKO vs SW480, $p < 0.001$; HCT116 vs SW480, $p < 0.001$).

To define its functional role, we established stable *CD276* knockdown (sh*CD276*) cell lines in HCT116 and RKO cells, with shNC as a control. Both Western blot and qPCR analyses confirmed efficient and sustained suppression of B7-H3 at the protein ($p < 0.001$; Fig. 1B,C) and mRNA levels ($p < 0.001$; Fig. 1D), validating these models for subsequent functional studies.

CD276 Knockdown Enhances Ferroptosis Sensitivity in Colorectal Cancer Cells

To determine whether B7-H3 regulates ferroptosis, we first assessed cellular morphology and ultrastructure following treatment with the ferroptosis inducer RSL3. Compared with shNC cells, sh*CD276* cells displayed reduced viability and pronounced cell shrinkage. Transmission electron microscopy revealed characteristic ferroptotic features, including mitochondrial shrinkage and increased membrane density. These alterations were further exacerbated upon RSL3 treatment (Fig. 2A,B). Consistently, CCK-8 assays showed that *CD276* knockdown significantly reduced cell viability in HCT116 cells ($p < 0.001$), with a further decrease following RSL3 treatment ($p < 0.001$), indicating increased ferroptosis sensitivity (Fig. 2C).

Given that ferroptosis is defined by lipid peroxidation and iron accumulation, we next quantified these biochemical hallmarks. Compared with shNC cells, sh*CD276* cells exhibited significantly elevated levels of malondialdehyde (MDA) and intracellular Fe^{2+} ($p < 0.05$), which were further increased upon RSL3 exposure ($p < 0.01$; Fig. 2D). To elucidate the underlying molecular changes, we analyzed ferroptosis-related gene expression. In HCT116 cells, *CD276* knockdown significantly upregulated *PTGS2*, *FTL*, and *FTH* mRNA ($p < 0.001$; Fig. 2E), while downregulating *GPX4* ($p < 0.001$). A similar expression pattern was observed in RKO cells, with increased *PTGS2*, *FTL*, and *FTH* ($p < 0.001$; Fig. 2F) and decreased *GPX4* expression ($p < 0.05$). Together, these findings indicate that *CD276* silencing promotes ferroptosis by enhancing lipid peroxidation, iron accumulation, and suppressing GPX4-mediated antioxidant defense.

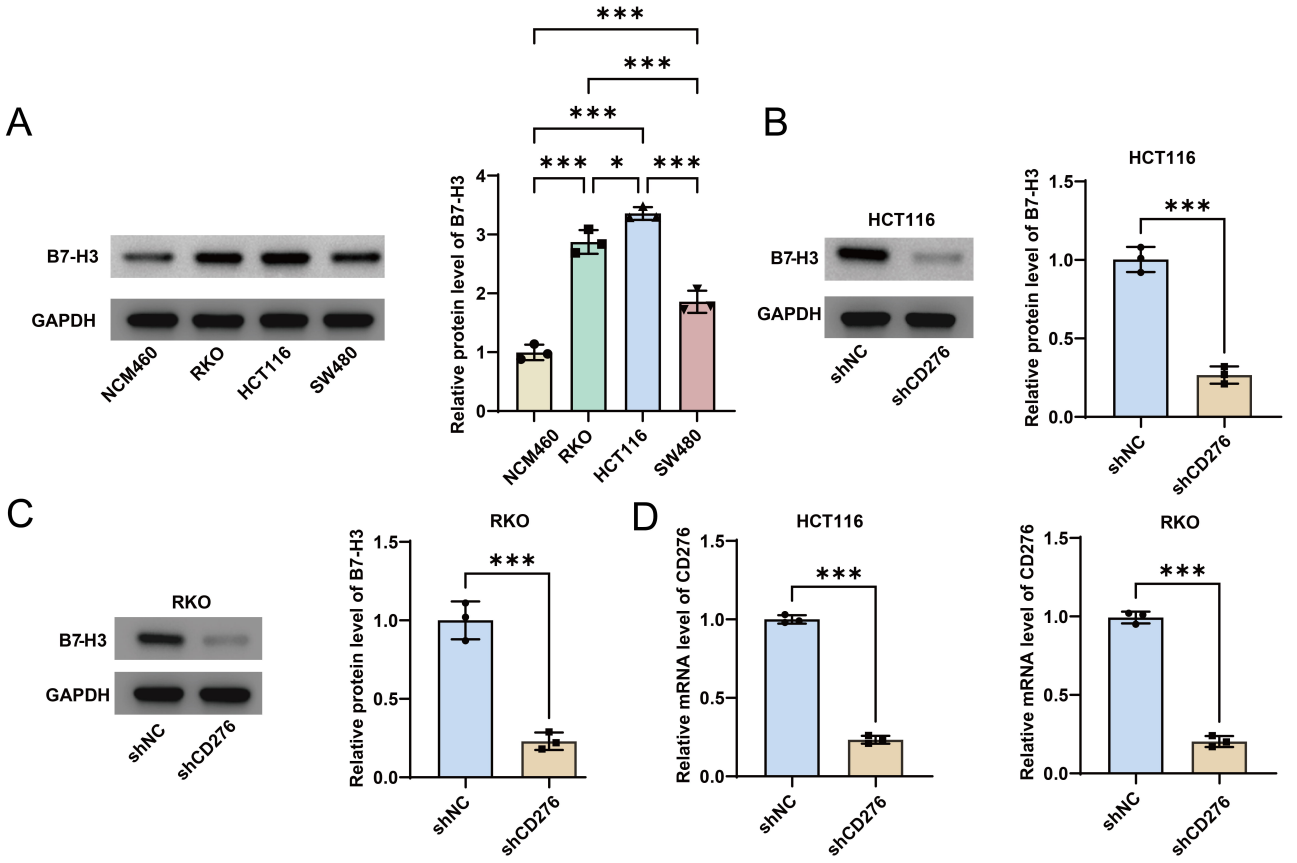

Fig. 1. B7-H3 is upregulated in colorectal cancer cell lines and validation of stable *CD276* knockdown. (A) Western blot analysis of B7-H3 protein expression in normal colonic epithelial NCM460 cells and colorectal cancer RKO, HCT116, and SW480 cells. (B,C) Western blot validation of B7-H3 protein knockdown efficiency by sh*CD276* in HCT116 (B) and RKO (C) cells. (D) qPCR analysis of *CD276* mRNA levels in HCT116 (left) and RKO (right) cells following *CD276* silencing. All *in vitro* experiments were performed in three independent biological replicates (n = 3). *$p < 0.05$, ***$p < 0.001$.

CD276 Overexpression Suppresses Ferroptosis and Modulates Cholesterol Metabolism

To further validate the role of B7-H3, we generated *CD276*-overexpressing (OE-*CD276*) HCT116 and RKO cell lines, with OE-NC as a control. Western blot and qPCR analyses confirmed robust upregulation of B7-H3 at both the protein ($p < 0.001$; Fig. 3A,B) and mRNA levels ($p < 0.001$; Fig. 3C).

Functionally, OE-*CD276* cells significantly increased viability compared with controls ($p < 0.001$; Fig. 3D). Upon RSL3 treatment, cell viability declined ($p < 0.001$), yet remained higher than in control cells, indicating enhanced resistance to ferroptosis. Biochemical analyses showed that OE-*CD276* cells significantly reduced MDA and Fe^{2+} levels relative to OE-NC cells ($p < 0.001$; Fig. 3E). Although RSL3 treatment increased these markers, their levels remained lower than in control conditions, suggesting that *CD276* overexpression attenuates lipid peroxidation and iron overload.

At the transcriptional level, OE-*CD276* significantly downregulated *PTGS2*, *FTL*, and *FTH* expression ($p < 0.001$; Fig. 3F), while upregulating *GPX4* ($p < 0.001$), exhibiting a pattern opposite to that observed upon *CD276* knockdown. These findings further support a suppressive role of B7-H3 in ferroptosis. Given the emerging link between cholesterol metabolism and ferroptosis, we next measured total cholesterol (TC) and LDL-C levels. *CD276* knockdown significantly increased TC and LDL-C levels ($p < 0.001$; Fig. 3G), whereas *CD276* overexpression reduced both parameters ($p < 0.01$), indicating that B7-H3 negatively regulates cholesterol metabolism in CRC cells. This metabolic modulation may contribute to its role in ferroptosis regulation.

Ferrostatin-1 Reverses B7-H3–Mediated Ferroptotic Phenotypes

To confirm that the observed cell death was ferroptosis-dependent, we performed rescue experiments using the ferroptosis inhibitor Ferrostatin-1 (Fer-1). In *CD276*-knockdown HCT116 cells, Fer-1 pretreatment significantly rescued RSL3-induced loss of cell viability, restoring viability from 23.20% to 90.27% ($p < 0.001$;

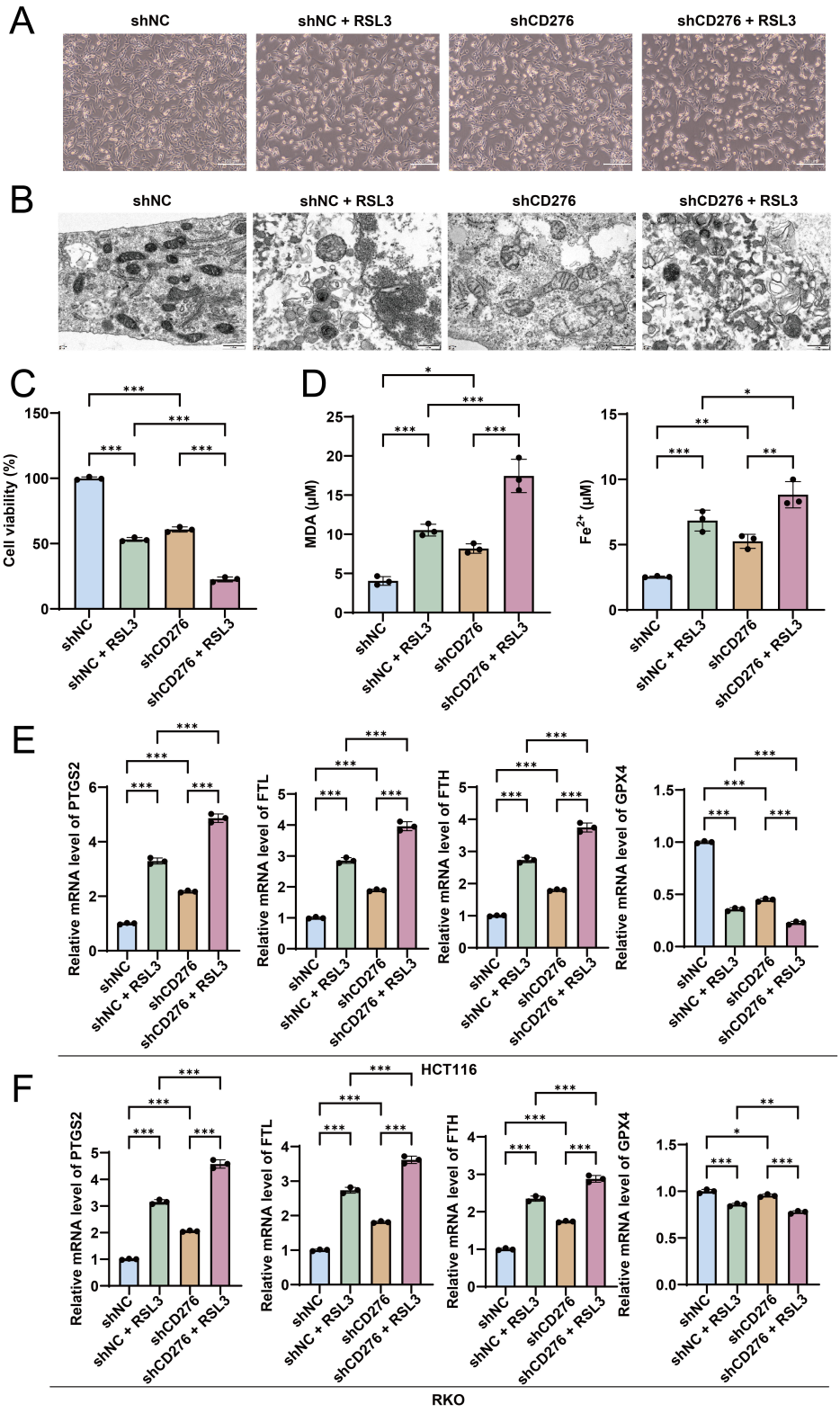

Fig. 2. *CD276* depletion sensitizes colorectal cancer cells to ferroptosis. (A) Representative bright-field microscopy images showing morphological alterations in HCT116 cells under shNC, sh*CD276*, or sh*CD276* + RSL3 treatment (scale bar: 100 μm). (B) Transmission electron microscopy (TEM) analysis of mitochondrial ultrastructural damage, a hallmark of ferroptosis, in HCT116 cells (scale bar: 500 nm). (C) CCK-8 assay for cell viability in HCT116 cells under the indicated treatments. (D) Colorimetric quantification of intracellular malondialdehyde (MDA) (left, TBARS assay) and Fe^{2+} (right) levels. (E,F) qPCR analysis of mRNA expression of ferroptosis-associated genes (*PTGS2*, *FTL*, *FTH*, *GPX4*) in HCT116 (E) and RKO (F) cells. All *in vitro* experiments were performed in three independent biological replicates (n = 3). *$p < 0.05$, **$p < 0.01$, ***$p < 0.001$.

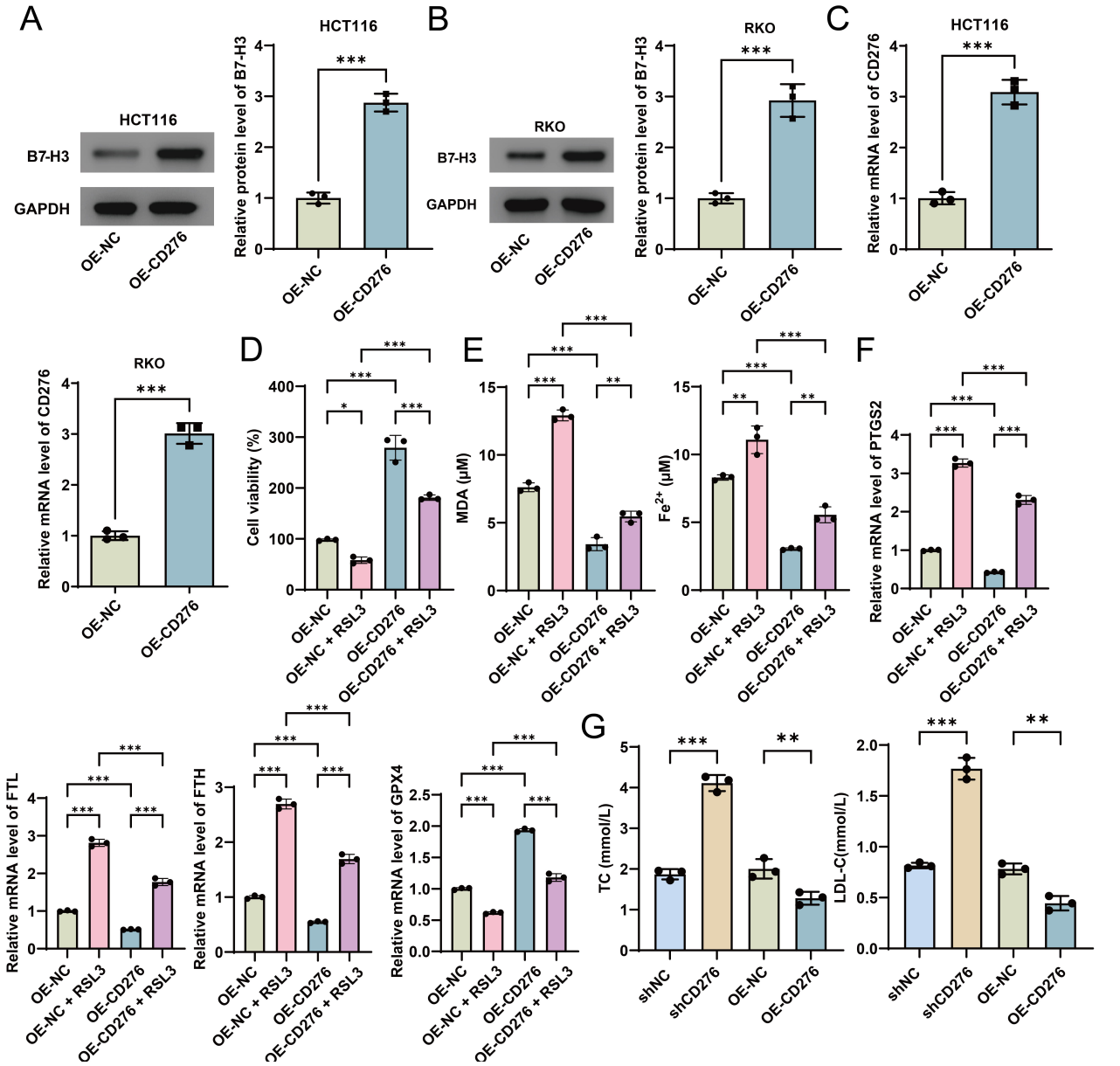

Fig. 3. *CD276* overexpression suppresses ferroptosis and modulates cholesterol metabolism in colorectal cancer cells. (A,B) Western blot validation of B7-H3 protein overexpression efficiency in HCT116 (A) and RKO (B) cells stably transduced with OE-*CD276*. (C) qPCR analysis of *CD276* mRNA levels in HCT116 and RKO cells following *CD276* overexpression. (D) CCK-8 assay assessing cell viability in HCT116 cells. (E) Colorimetric quantification of intracellular MDA (TBAR assay) and Fe^{2+} levels in HCT116 cells. (F) qPCR analysis of mRNA expression of ferroptosis-associated genes (*PTGS2*, *FTL*, *FTH*, *GPX4*) in HCT116 cells. (G) Colorimetric measurement of total cholesterol (TC) and low-density lipoprotein cholesterol (LDL-C) levels in HCT116 cells under indicated treatments. $^{*}p < 0.05$, $^{**}p < 0.01$, $^{***}p < 0.001$. All *in vitro* assays were performed in three independent biological replicates (n = 3).

Fig. 4A). Concurrently, Fer-1 markedly reduced elevated MDA and Fe^{2+} levels induced by RSL3 ($p < 0.001$). In *CD276*-overexpressing cells, Fer-1 further enhanced resistance to ferroptosis, significantly reversing RSL3-induced decreases in viability and increases in MDA and Fe^{2+} ($p < 0.001$; Fig. 4B). Collectively, these findings demonstrate that B7-H3–mediated regulation of cell death in CRC is ferroptosis-dependent and can be effectively reversed by pharmacological inhibition of ferroptosis.

B7-H3 Engages PI3K p85 to Activate the PI3K/AKT/SREBP2 Axis, Thereby Regulating Cholesterol Metabolism and Ferroptosis in Colorectal Cancer

To delineate the molecular mechanism by which B7-H3 regulates cholesterol metabolism and ferroptosis, we systematically interrogated its upstream signaling cascade in HCT116 cells. Competitive ELISA revealed that *CD276* knockdown markedly reduced PI3K kinase ac-

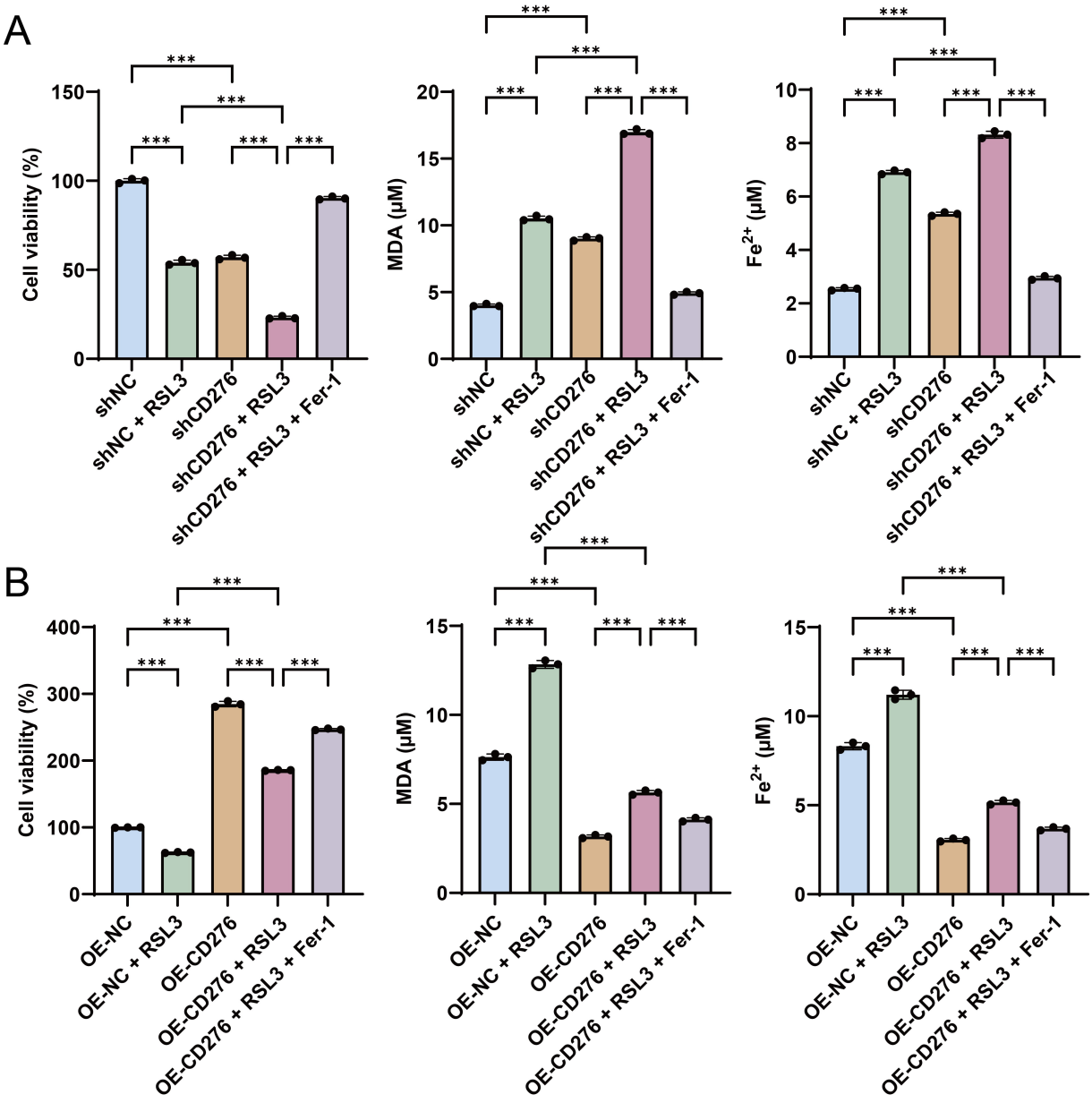

Fig. 4. Ferrostatin-1 rescues colorectal cancer cells from B7-H3-mediated ferroptosis resistance. (A) Cell viability, intracellular MDA content, and Fe^{2+} levels in shNC and sh*CD276* HCT116 cells treated with RSL3, with or without Ferrostatin-1 (Fer-1) pretreatment. (B) Cell viability, intracellular MDA content, and Fe^{2+} levels in OE-NC and OE-*CD276* HCT116 cells treated with RSL3, with or without Fer-1 pretreatment. All assays were performed in three independent biological replicates (n = 3). ***$p < 0.001$.

tivity, whereas *CD276* overexpression significantly enhanced PI3K activity (both $p < 0.001$; Fig. 5A). Co-immunoprecipitation (Co-IP) assays further demonstrated a direct interaction between B7-H3 and the PI3K regulatory subunit p85. In Flag-tagged *CD276*–overexpressing HCT116 cells, Flag immunoprecipitation specifically enriched B7-H3 and co-precipitated PI3K p85, while no specific bands were detected in the IgG control. Reciprocal IP using a p85 antibody confirmed the presence of endogenous B7-H3 in the precipitated complex (Fig. 5B), establishing that B7-H3 physically associates with PI3K p85 to promote its kinase activity.

We next focused on sterol regulatory element-binding protein 2 (SREBP2), a key transcription factor governing cholesterol biosynthesis, to delineate the downstream signaling cascade. Western blot analysis showed that CD276 knockdown significantly decreased the p-AKT/AKT ratio while increasing nuclear SREBP2 (n-SREBP2) levels, whereas *CD276* overexpression produced the opposite effects ($p < 0.01$; Fig. 5C,D). These findings indicate that B7-H3 activates AKT signaling to suppress SREBP2 activation. Functional rescue experiments substantiated this regulatory axis. Treatment with the SREBP2 inhibitor betulin effectively reversed the increases in TC and LDL-C induced

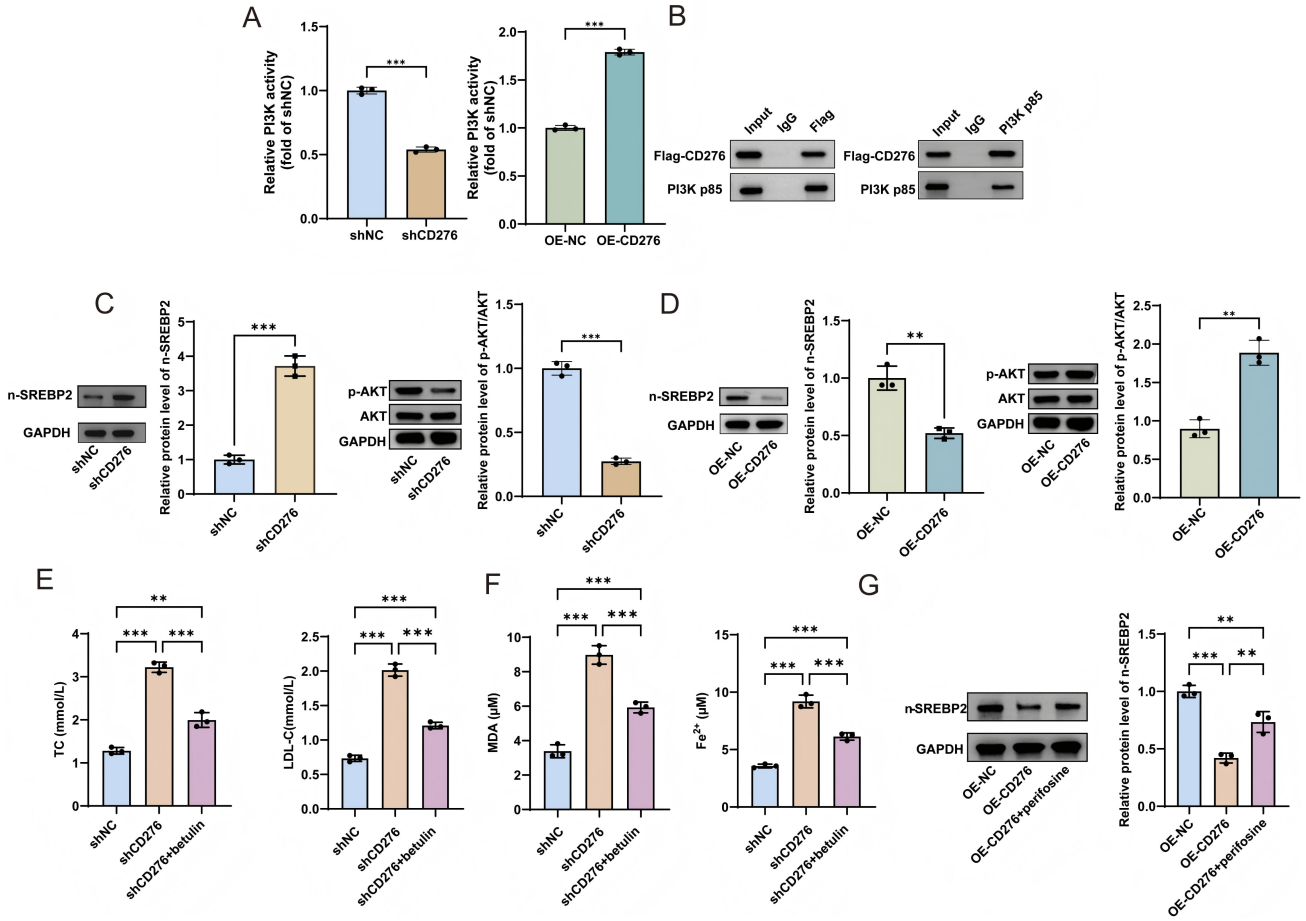

Fig. 5. B7-H3 governs cholesterol metabolism and ferroptosis via the AKT/SREBP2 axis in colorectal cancer cells. (A) Competitive ELISA for PI3K kinase activity in shNC/sh*CD276* and OE-NC/OE-*CD276* HCT116 cells. (B) Co-immunoprecipitation (Co-IP) confirming the physical interaction between B7-H3 and the PI3K p85 regulatory subunit in Flag-tagged *CD276*-overexpressing HCT116 cells. Forward IP was performed with anti-Flag antibody, reverse IP with anti-p85 antibody; isotype IgG served as a negative control. (C,D) Western blot analysis of nuclear SREBP2 (n-SREBP2) and p-AKT protein levels in HCT116 cells following *CD276* knockdown (C) or overexpression (D). (E) Colorimetric quantification of TC and LDL-C levels in HCT116 cells under shNC, sh*CD276*, or sh*CD276*+betulin treatment. (F) Intracellular MDA and Fe^{2+} levels measured by TBAR and colorimetric assays, respectively. (G) Western blot analysis of n-SREBP2 protein levels in OE-NC, OE-*CD276*, and OE-*CD276*+perifosine-treated HCT116 cells. All assays were performed in three independent biological replicates (n = 3). $^{**}p < 0.01$, $^{***}p < 0.001$.

by *CD276* knockdown, and concurrently reduced MDA and Fe^{2+} levels ($p < 0.001$; Fig. 5E,F), confirming SREBP2 as a critical downstream effector mediating cholesterol metabolism and ferroptosis. Conversely, the AKT inhibitor perifosine significantly restored n-SREBP2 expression in *CD276*-overexpressing cells ($p < 0.01$; Fig. 5G), further establishing AKT as an upstream regulator linking B7-H3 to SREBP2. Collectively, these results define a B7-H3–PI3K p85–AKT–SREBP2 signaling axis that integrates cholesterol metabolism with ferroptosis regulation in CRC cells.

CD276 Knockdown Suppresses Tumor Growth Under High-Cholesterol Conditions by Activating the SREBP2–Ferroptosis Axis In Vivo

To validate these findings *in vivo*, we first established a high-cholesterol diet mouse model. Compared with mice fed a standard diet, those receiving a high-cholesterol diet exhibited significantly elevated serum total cholesterol (TC), LDL-C levels, and hepatic TC content (all $p < 0.001$; Fig. 6A), confirming successful induction of a hypercholesterolemic state that recapitulates a metabolically altered tumor microenvironment. In xenograft experiments, tumors derived from sh*CD276* HCT116 cells displayed markedly reduced growth compared with shNC controls throughout the observation period (days 0–27; Fig. 6B,C). Two-way ANOVA demonstrated significant effects of time, group, and their interaction (time × group: $F = 33.87$, $p < 0.001$; time: $F = 105.4$, $p < 0.001$; group: $F = 32.09$, $p < 0.01$), indicating that *CD276* knockdown robustly suppresses tumor progression under high-cholesterol conditions. At the endpoint, tumor weights were also significantly lower in the sh*CD276* group ($p < 0.01$; Fig. 6C).

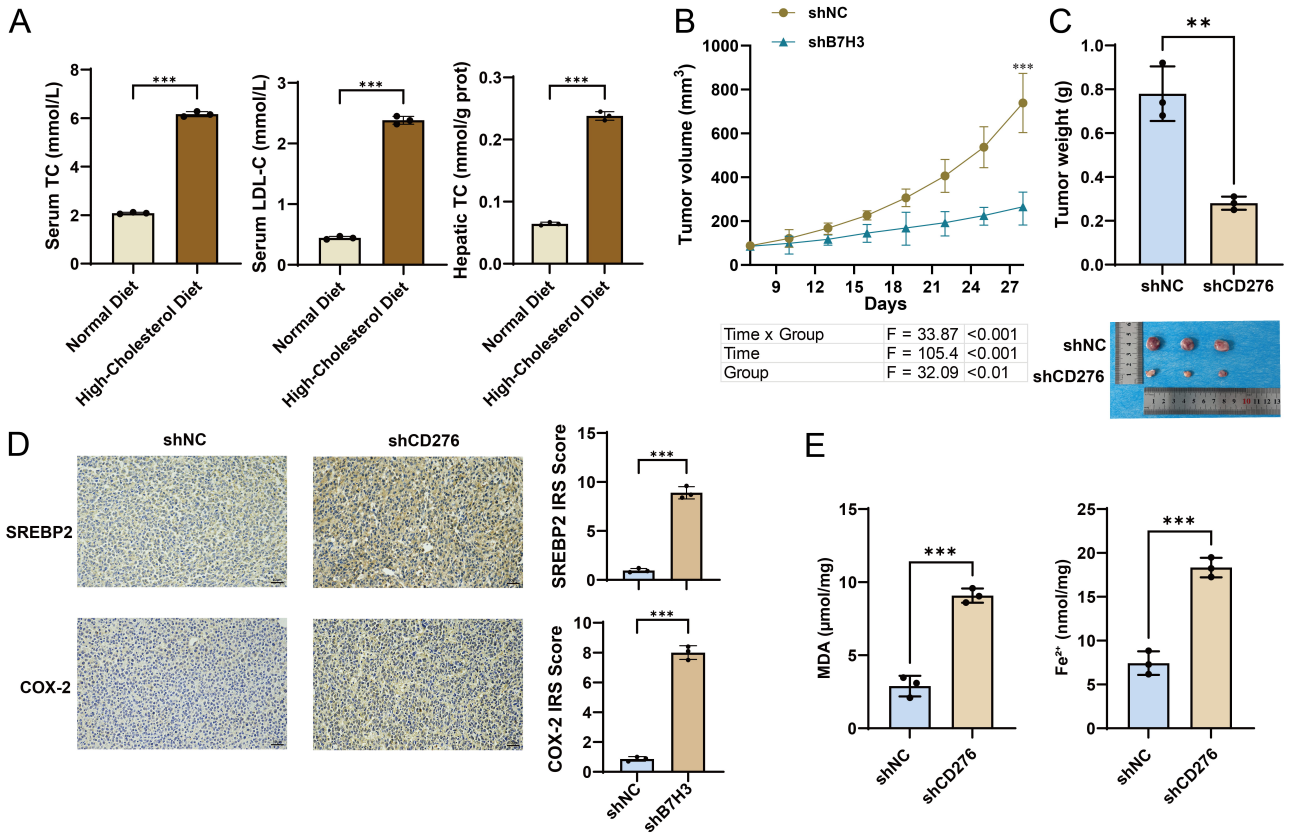

Fig. 6. *CD276* depletion restrains colorectal cancer growth by activating the SREBP2/ferroptosis axis under a high-cholesterol diet *in vivo*. (A) Serum TC, serum LDL-C, and hepatic TC levels in BALB/c nude mice fed a normal or high-cholesterol diet for 27 days (n = 6 per group). (B) Tumor volume growth curves of shNC and sh*CD276* xenografts from day 0 to day 27. ***$p < 0.001$ vs shNC. (C) Tumor weight and representative images of shNC and sh*CD276* xenografts at the experimental endpoint. (D) Immunohistochemical (IHC) staining of SREBP2 and COX-2 in shNC and sh*CD276* tumor tissues (scale bar: 50 μm). (E) Intratumoral MDA and Fe^{2+} levels measured by TBAR and colorimetric assays. **$p < 0.01$, ***$p < 0.001$.

Immunohistochemical analysis revealed significantly increased staining intensity of SREBP2 and COX-2 in sh*CD276* tumors compared with controls (Fig. 6D), suggesting enhanced activation of cholesterol regulatory and ferroptosis-associated pathways *in vivo*. Consistently, biochemical analyses demonstrated that MDA levels and Fe^{2+} concentrations were markedly elevated in sh*CD276* tumors ($p < 0.001$; Fig. 6E), indicating increased lipid peroxidation and iron accumulation.

Together, these findings demonstrate that *CD276* knockdown suppresses CRC tumor growth *in vivo* by activating the SREBP2-driven ferroptosis axis, particularly under conditions of dysregulated cholesterol metabolism.

Discussion

This study focused on the non-immune functions of B7-H3, systematically investigating its role in regulating ferroptosis and cholesterol metabolism in CRC cells, and elucidating the underlying molecular mechanisms. Using *in vivo* experiments, we further validated its impact on tumor growth, aiming to provide a mechanistic basis and potential therapeutic target for CRC. We demonstrate that B7-H3 is aberrantly overexpressed in CRC cells and suppresses cholesterol metabolism via the AKT/SREBP2 signaling axis, thereby inhibiting ferroptosis and promoting CRC proliferation both *in vitro* and *in vivo*. Under high-cholesterol dietary conditions, *CD276* knockdown significantly restrains xenograft tumor growth through activation of the SREBP2/ferroptosis axis, highlighting B7-H3 as a central regulator at the intersection of CRC metabolism and cell death.

Consistent with prior studies, B7-H3 (*CD276*) is highly expressed across multiple malignancies while remaining low in normal tissues [11]. In our experiments, B7-H3 protein levels in RKO, HCT116, and SW480 CRC cell lines were markedly elevated compared with normal colonic epithelial NCM460 cells, displaying notable cell line–specific heterogeneity: HCT116 cells exhibited the highest expression, followed by RKO and then SW480. This finding aligns with previous reports; for example, Ma *et al.* [14] observed that B7-H3 expression in RKO,

HCT116, HT29, and SW480 cells consistently exceeded that in normal colonic cells. Clinical studies further indicate that over half of CRC patient tumors exhibit high B7-H3 expression [15]. Beyond CRC, elevated B7-H3 has been reported in malignancies such as non-small cell lung cancer (NSCLC), where it correlates with lymph node metastasis and advanced disease stage [16], suggesting that its aberrant expression may contribute to tumor invasiveness, metastatic potential, and poor prognosis.

B7-H3, a member of the B7 family of immune costimulatory/inhibitory molecules, has been shown to suppress T cell activation and facilitate tumor immune evasion across multiple malignancies [17–19]. Consistent with these immunological roles, our study confirmed high B7-H3 expression in CRC cells; however, we primarily focused on its non-immune functions. Emerging evidence indicates that B7-H3 also contributes to tumor metabolic reprogramming—for example, by promoting lactate metabolism and HK2 expression [20]—underscoring its functional versatility. Here, we systematically investigated B7-H3's regulation of both metabolism and cell death in CRC, offering novel mechanistic insight into its non-immune roles.

Ferroptosis is a distinct form of regulated cell death characterized by iron-dependent lipid peroxidation, mechanistically and morphologically different from apoptosis or necrosis [21]. Its execution relies on the loss of glutathione peroxidase 4 (*GPX4*) activity, resulting in excessive peroxidation of polyunsaturated phospholipids and subsequent cell death [21]. Hallmarks of ferroptosis include glutathione depletion, elevated labile Fe^{2+}, and accumulation of lipid peroxides such as MDA, accompanied by upregulation of *PTGS2* (a ferroptosis marker) and *FTL/FTH* (iron storage genes), and downregulation of *GPX4* (a key ferroptosis suppressor) [22,23]. In our study, *CD276* knockdown markedly decreased CRC cell viability, with concomitant increases in intracellular MDA and Fe^{2+}, indicating enhanced lipid peroxidation and iron accumulation. mRNA levels of P*TGS2, FTL*, and *FTH* were significantly elevated, whereas *GPX4* expression was notably reduced in HCT116 cells. These changes are consistent with canonical ferroptosis mechanisms: *PTGS2* upregulation and diminished GSH/GPX4 activity indicate activation of the ferroptotic program [21]. Interestingly, *GPX4* levels in RKO cells remained largely unchanged, reflecting inter-cell line heterogeneity. Even within the ferroptosis pathway, different CRC cell lines may partially compensate for *GPX4* loss through alternative antioxidant systems, thereby mitigating its downregulation. Such variability in gene expression and environmental adaptation has been reported in tumors and may account for the differential phenotypic outcomes following gene perturbation.

Conversely, *CD276* overexpression produced an opposite phenotype: enhanced cell viability, reduced MDA and Fe^{2+}, decreased *PTGS2* and *FTL/FTH* expression, and upregulated *GPX4* (in HCT116). To confirm that these effects were specific to ferroptosis rather than general cytotoxicity, OE-*CD276* cells were treated with RSL3, a *GPX4*-specific inhibitor. Compared with OE-NC controls, OE-*CD276* cells displayed significantly reduced sensitivity to RSL3-induced cell death, demonstrating that B7-H3 specifically modulates the ferroptotic pathway. Because RSL3 directly inhibits *GPX4* to induce ferroptosis [21], resistance in OE-*CD276* cells confirms that B7-H3's effect is ferroptosis-specific rather than attributable to apoptosis or necrosis. B7-H3-mediated regulation of ferroptosis was paralleled by substantial changes in cellular cholesterol levels. *CD276* knockdown increased total cholesterol (TC) and LDL-C, whereas *CD276* overexpression reduced these levels. Notably, these alterations were directionally consistent with ferroptotic phenotypes: ferroptosis was enhanced when cholesterol was elevated (sh*CD276*) and suppressed when cholesterol was reduced (OE). Dysregulated cholesterol metabolism is a recognized hallmark of CRC, and clinical studies link hyperlipidemia (elevated TC and LDL-C) to CRC development. Cholesterol is a major component of cellular membranes, modulating membrane fluidity and the assembly of signaling complexes [24]. High cholesterol promotes CRC proliferation and invasion via *PI3K/AKT* signaling [25,26] and can suppress lipid peroxidation by reducing membrane fluidity [8,27]. Collectively, these observations suggest that B7-H3 may inhibit ferroptosis by suppressing cholesterol biosynthesis, thereby limiting the availability of membrane lipid substrates for peroxidation, whereas *CD276* knockdown increases cholesterol levels, enhancing substrate availability and promoting ferroptosis.

The *AKT* pathway is a well-characterized pro-oncogenic signaling axis that regulates diverse metabolic and growth processes [28]. Reduced Akt activity impairs the ER-to-Golgi transport of SREBP2, thereby inhibiting its nuclear activity [29]. SREBP2 is the master transcription factor for cholesterol biosynthesis, and its activation upregulates key enzymes such as HMGCR, increasing TC and LDL-C synthesis [30,31]. In this study, *CD276* knockdown decreased p-AKT/AKT ratios while enhancing nuclear (active) SREBP2 levels. Conversely, *CD276* overexpression increased p-AKT/AKT and reduced nuclear SREBP2, establishing a "B7-H3 $\rightarrow$ AKT $\rightarrow$ SREBP2" regulatory axis. Pharmacological validation confirmed this chain: treatment of *CD276*-knockdown cells with the SREBP2 inhibitor betulin reduced TC and LDL-C, and simultaneously decreased MDA and Fe^{2+} levels, demonstrating that SREBP2 inhibition reverses the metabolic dysregulation and ferroptotic enhancement induced by *CD276* loss. Similarly, AKT inhibition (perifosine) in *CD276*-overexpressing cells restored nuclear SREBP2 levels, confirming AKT's upstream role in B7-H3–mediated suppression of SREBP2.

Collectively, these results define a coherent regulatory axis: B7-H3 promotes AKT phosphorylation, which in turn suppresses SREBP2 nuclear localization and activ-

ity. Reduced SREBP2 activity downregulates the expression of cholesterol biosynthetic genes, leading to decreased intracellular TC and LDL-C levels. The resulting reduction in cholesterol substrates limits lipid peroxidation and lowers the labile iron pool, thereby inhibiting ferroptosis, as evidenced by decreased MDA and Fe^{2+}, downregulated PTGS2, and upregulated GPX4. This cascade ultimately enhances CRC cell proliferation and survival. Conversely, *CD276* knockdown diminishes AKT activity, activates SREBP2, and elevates cholesterol biosynthesis, increasing lipid peroxidation substrates and iron load, thereby amplifying ferroptosis and suppressing tumor growth. While previous research has primarily focused on AKT/SREBP2 regulation of tumor lipid metabolism and proliferation [31], our findings introduce the immune checkpoint molecule B7-H3 into this network, expanding the molecular map of metabolism–cell death crosstalk in CRC and providing a framework for combinatorial metabolic and immune-targeted therapies.

In a xenograft model established under a high-cholesterol diet, tumors from *CD276*-knockdown mice significantly reduced volume and weight compared with controls, with intergroup differences widening over time (two-way ANOVA, significant interaction). Immunohistochemistry of tumor tissues markedly increased SREBP2 and ferroptosis activation marker COX-2 in the sh*CD276* group, accompanied by elevated tumor MDA and Fe^{2+} levels, corroborating *in vitro* observations. These *in vivo* results demonstrate that, under a high-cholesterol microenvironment, *CD276* knockdown suppresses tumor growth via activation of the SREBP2/ferroptosis axis, consistent with cell-based experiments and reinforcing the robustness of our conclusions.

This study has several limitations that warrant further investigation. First, the cell line panel was limited to RKO, HCT116, and SW480; primary CRC cells were not examined, which may constrain generalizability. Validation in primary CRC cells is needed to strengthen the universality of B7-H3's regulatory role. Second, mechanistic insights were restricted to B7-H3-mediated AKT activation and SREBP2 inhibition; upstream regulators of AKT activation by B7-H3, including its potential receptors and adaptor molecules, remain undefined. Third, the *in vivo* experiments were conducted in immunodeficient nude mice, precluding analysis of potential crosstalk between B7-H3-mediated immune modulation and ferroptosis regulation. Immunocompetent mouse models are required to clarify B7-H3's dual role in CRC immune evasion and metabolic reprogramming. Fourth, clinical correlation remains unaddressed: we did not assess the relationship among B7-H3, SREBP2, ferroptosis, and cholesterol metabolism in patient CRC samples, nor their association with clinicopathological features. Expanding the analyses to large clinical samples will be essential to evaluate the translational relevance of our findings.

Conclusions

In summary, B7-H3 is aberrantly overexpressed in CRC cells and suppresses cholesterol metabolism via the AKT/SREBP2 axis, thereby inhibiting ferroptosis and promoting CRC proliferation both *in vitro* and *in vivo*. These effects can be reversed by SREBP2 or AKT inhibitors. In high-cholesterol diet xenograft models, *CD276* knockdown significantly inhibits tumor growth while activating the SREBP2/ferroptosis axis. The B7-H3/SREBP2/AKT pathway represents a potential therapeutic target in CRC, providing a mechanistic rationale for metabolic and ferroptosis-targeted interventions, although further studies are required to validate its clinical utility.

Availability of Data and Materials

The datasets generated and analyzed during the current study can be obtained from the corresponding author upon reasonable request.

Author Contributions

CL and QZ conceived and designed the study. CL, QJ and YS performed the experiments and collected the data. CL and QJ conducted data analysis and interpretation. QZ provided critical guidance on study design and supervised the overall project. CL drafted the manuscript. QZ, QJ and YS critically revised the manuscript for important intellectual content. All authors read and approved the final manuscript. All authors have participated sufficiently in the work and agreed to be accountable for all aspects of the work.

Ethics Approval and Consent to Participate

All animal experiments were conducted in accordance with institutional guidelines and approved by the Institutional Animal Care and Use Committee of the Affiliated Hospital of Nantong University (Approval No. 2025-L139). All procedures complied with the ARRIVE Guidelines 2.0 and were performed in accordance with relevant national and international regulations for the care and use of laboratory animals.

Acknowledgment

Not applicable.

Funding

This research received no external funding.

Conflict of Interest

The authors declare no conflict of interest.

References

[1] Yin Y, Zhang X. Correction: Analysis of trends in the burden of colorectal cancer in China and globally from 1990 to 2021 with projections for the next 15 years: a cross-sectional study based on the GBD database. Frontiers in Public Health. 2025; 13: 1635228. https://doi.org/10.3389/fpubh.2025.1635228.

[2] Wu S, Zhang Y, Lin Z, Wei M. Global burden of colorectal cancer in 2022 and projections to 2050: incidence and mortality estimates from GLOBOCAN. BMC Cancer. 2025; 25: 1770. https://doi.org/10.1186/s12885-025-15138-0.

[3] Tang YL, Li DD, Duan JY, Sheng LM, Wang X. Resistance to targeted therapy in metastatic colorectal cancer: Current status and new developments. World Journal of Gastroenterology. 2023; 29: 926–948. https://doi.org/10.3748/wjg.v29.i6.926.

[4] Xie YH, Chen YX, Fang JY. Comprehensive review of targeted therapy for colorectal cancer. Signal Transduction and Targeted Therapy. 2020; 5: 22. https://doi.org/10.1038/s41392-020-0116-z.

[5] Wang S, Guo Q, Zhou L, Xia X. Ferroptosis: A double-edged sword. Cell Death Discovery. 2024; 10: 265. https://doi.org/10.1038/s41420-024-02037-9.

[6] Yang L, Zhang Y, Zhang Y, Fan Z. Mechanism and application of ferroptosis in colorectal cancer. Biomedicine & Pharmacotherapy. 2023; 158: 114102. https://doi.org/10.1016/j.biopha.2022.114102.

[7] Cheng X, Zhao F, Ke B, Chen D, Liu F. Harnessing Ferroptosis to Overcome Drug Resistance in Colorectal Cancer: Promising Therapeutic Approaches. Cancers. 2023; 15: 5209. https://doi.org/10.3390/cancers15215209.

[8] Sun Q, Liu D, Cui W, Cheng H, Huang L, Zhang R, *et al*. Cholesterol mediated ferroptosis suppression reveals essential roles of Coenzyme Q and squalene. Communications Biology. 2023; 6: 1108. https://doi.org/10.1038/s42003-023-05477-8.

[9] Larkin B, Nishizaki D, Miyashita H, Lee S, Nikanjam M, Eskander RN, *et al*. B7-H3/CD276: Novel Immune Checkpoint and Jack of All Trades. ImmunoTargets and Therapy. 2025; 14: 967–977. https://doi.org/10.2147/ITT.S534666.

[10] Lu Z, Zhao ZX, Cheng P, Huang F, Guan X, Zhang MG, *et al*. B7-H3 immune checkpoint expression is a poor prognostic factor in colorectal carcinoma. Modern Pathology: an Official Journal of the United States and Canadian Academy of Pathology, Inc. 2020; 33: 2330–2340. https://doi.org/10.1038/s41379-020-0587-z.

[11] Varghese E, Samuel SM, Brockmueller A, Shakibaei M, Kubatka P, Büsselberg D. B7-H3 at the crossroads between tumor plasticity and colorectal cancer progression: a potential target for therapeutic intervention. Cancer Metastasis Reviews. 2024; 43: 115–133. https://doi.org/10.1007/s10555-023-10137-8.

[12] Su H, Peng C, Liu Y. Regulation of ferroptosis by PI3K/Akt signaling pathway: a promising therapeutic axis in cancer. Frontiers in Cell and Developmental Biology. 2024; 12: 1372330. https://doi.org/10.3389/fcell.2024.1372330.

[13] You W, Su L, Weng S, Li J, Wang X, Liang B, *et al*. SREBP-2 promotes cancer progression through the mevalonate-Akt pathway in non-small cell lung cancer. Scientific Reports. 2025; 15: 23103. https://doi.org/10.1038/s41598-025-07437-0.

[14] Ma Y, Wang R, Lu H, Li X, Zhang G, Fu F, *et al*. B7-H3 promotes the cell cycle-mediated chemoresistance of colorectal cancer cells by regulating CDC25A. Journal of Cancer. 2020; 11: 2158–2170. https://doi.org/10.7150/jca.37255.

[15] Parente P, Ciardiello D, Angerilli V, Gasparello J, Fassan M. B7-H3 in Colorectal Adenocarcinoma: Are We Focusing on the Right Target? Clinical Colorectal Cancer. 2025; 24: 492–497. https://doi.org/10.1016/j.clcc.2025.09.005.

[16] Zhao S, Zhang H, Shang G. Research progress of B7-H3 in malignant tumors. Frontiers in Immunology. 2025; 16: 1586759. https://doi.org/10.3389/fimmu.2025.1586759.

[17] Malapelle U, Parente P, Pepe F, Di Micco MC, Russo A, Clemente C, *et al*. B7-H3/CD276 Inhibitors: Is There Room for the Treatment of Metastatic Non-Small Cell Lung Cancer? International Journal of Molecular Sciences. 2022; 23: 16077. https://doi.org/10.3390/ijms232416077.

[18] Zhou WT, Jin WL. B7-H3/CD276: An Emerging Cancer Immunotherapy. Frontiers in Immunology. 2021; 12: 701006. https://doi.org/10.3389/fimmu.2021.701006.

[19] Zhao B, Li H, Xia Y, Wang Y, Wang Y, Shi Y, *et al*. Immune checkpoint of B7-H3 in cancer: from immunology to clinical immunotherapy. Journal of Hematology & Oncology. 2022; 15: 153. https://doi.org/10.1186/s13045-022-01364-7.

[20] Zhang T, Jin Y, Jiang X, Li L, Qi X, Mao Y, *et al*. Clinical and Prognostic Relevance of B7-H3 and Indicators of Glucose Metabolism in Colorectal Cancer. Frontiers in Oncology. 2020; 10: 546110. https://doi.org/10.3389/fonc.2020.546110.

[21] Yang WS, Stockwell BR. Ferroptosis: Death by Lipid Peroxidation. Trends in Cell Biology. 2016; 26: 165–176. https://doi.org/10.1016/j.tcb.2015.10.014.

[22] Ru Q, Li Y, Chen L, Wu Y, Min J, Wang F. Iron homeostasis and ferroptosis in human diseases: mechanisms and therapeutic prospects. Signal Transduction and Targeted Therapy. 2024; 9: 271. https://doi.org/10.1038/s41392-024-01969-z.

[23] Jin X, Tang J, Qiu X, Nie X, Ou S, Wu G, *et al*. Ferroptosis: Emerging mechanisms, biological function, and therapeutic potential in cancer and inflammation. Cell Death Discovery. 2024; 10: 45. https://doi.org/10.1038/s41420-024-01825-7.

[24] Mollinedo F, Gajate C. Lipid rafts as signaling hubs in cancer cell survival/death and invasion: implications in tumor progression and therapy: Thematic Review Series: Biology of Lipid Rafts. Journal of Lipid Research. 2020; 61: 611–635. https://doi.org/10.1194/jlr.TR119000439.

[25] Xie X, Wang W, Zhang H, Zhao S, Zhang N, Gao Y, *et al*. Cholesterol-induced colorectal cancer progression and its mitigation through gut microbiota remodeling and simvastatin treatment. BMC Cancer. 2025; 25: 977. https://doi.org/10.1186/s12885-025-14379-3.

[26] Chen X, Ma Z, Yi Z, Wu E, Shang Z, Tuo B, *et al*. The effects of metabolism on the immune microenvironment in colorectal cancer. Cell Death Discovery. 2024; 10: 118. https://doi.org/10.1038/s41420-024-01865-z.

[27] Zhao X, Lian X, Xie J, Liu G. Accumulated cholesterol protects tumours from elevated lipid peroxidation in the microenvironment. Redox Biology. 2023; 62: 102678. https://doi.org/10.1016/j.redox.2023.102678.

[28] Jiang M, Zhang K, Zhang Z, Zeng X, Huang Z, Qin P, *et al*. PI3K/AKT/mTOR Axis in Cancer: From Pathogenesis to Treatment. MedComm. 2025; 6: e70295. https://doi.org/10.1002/mco2.70295.

[29] Mohamed A, Viveiros A, Williams K, Posse de Chaves E. Aβ inhibits SREBP-2 activation through Akt inhibition. Journal of Lipid Research. 2018; 59: 1–13. https://doi.org/10.1194/jlr.M076703.

[30] Madison BB. Srebp2: A master regulator of sterol and fatty acid synthesis. Journal of Lipid Research. 2016; 57: 333–335. https://doi.org/10.1194/jlr.C066712.

[31] Fan M, Chen Z, Shao W, Chen Y, Lin Z, Yi C, *et al*. SREBP2 inhibitor betulin sensitizes hepatocellular carcinoma to lenvatinib by inhibiting the mTOR/IL-1β pathway. Acta Biochimica et Biophysica Sinica. 2023; 55: 1479–1486. https://doi.org/10.3724/abbs.2023122.